Study of the epitaxy between -Fe 2O3 , hematite and spinel in brown-glazed Chinese ceramics using electron diffraction mapping techniques

Clément Holé, Magali Brunet, Sébastien Joulié, Zhao Ren, Tian Wang, Gilles Wallez, Philippe Sciau

JOURNAL OF APPLIED CRYSTALLOGRAPHY

ISSN 1600-5767

Study of the epitaxy between ε-Fe_2O_3, hematite and spinel in brown-glazed Chinese ceramics using electron diffraction mapping techniques

Clément Holé,[a]* Magali Brunet,[a] Sébastien Joulié,[a] Zhao Ren,[b] Tian Wang,[b] Gilles Wallez[c,d] and Philippe Sciau[a]*

[a]CNRS, CEMES, University of Toulouse, Toulouse, 31055, France, [b]Institute of Silicate Cultural Heritage, School of Material Science and Engineering, Shaanxi Key Laboratory of Green Preparation and Functionalization for Inorganic Materials, Shaanxi University of Science and Technology, Xi'an, 710021, People's Republic of China, [c]CNRS, Institut de Recherche de Chimie Paris, Chimie ParisTech, PSL Research University, Paris, 75005, France, and [d]UFR 926, Sorbonne University, Paris, 75005, France. *Correspondence e-mail: clement.hole@alumni.chimieparistech.psl.eu, philippe.sciau@cemes.fr

Received 24 August 2023
Accepted 14 February 2024

Edited by G. J. McIntyre, Australian Nuclear Science and Technology Organisation, Lucas Heights, Australia

Keywords: ε-Fe_2O_3; hematite; spinel; epitaxy; TKD; transmission Kikuchi diffraction; ACOM-PED; automated crystal orientation mapping–precession electron diffraction; brown glaze.

Supporting information: this article has supporting information at journals.iucr.org/j

Black-to-brown Chinese ceramics have sparked the interest of material scientists since the widespread discovery of complex dendritic structures containing mainly the rare ε-Fe_2O_3 polymorph in their glazes. This study proposes to tackle this issue using two electron diffraction mapping techniques, transmission Kikuchi diffraction and automated crystal orientation mapping–precession electron diffraction, which have not been fully exploited despite their relevance for studying these structures at the scales of interest. It first demonstrates the efficiency of applying these techniques to characterize the structures at the nanoscale and discusses some limitations that may be encountered, in particular due to the specificity of heritage samples. It then focuses on the crystalline orientations obtained with these techniques, which highlight epitaxial relationships among the crystalline planes (001) of the ε-Fe_2O_3 phase, (0001) of the hematite and (111) of the spinel. Finally, it discusses the growth of such complex multi-phase structures by proposing two possible mechanisms, one based on the transformation of ε-Fe_2O_3 into hematite and spinel, and the other based on the growth of hematite and spinel on already crystallized ε-Fe_2O_3 dendrites. It also compares the dendritic structures of the two modern samples with those found in an ancient sample of Jian ware.

1. Introduction

The scientific characterization of materials that make up ancient artefacts has developed significantly in recent years in order to document the history of techniques developed by different civilizations. To better understand these ancient materials, accurate identification of the crystalline phases composing them is crucial as it can lead to key information about the manufacturing processes of the objects as a whole. However, the use of non-purified raw materials by the ancient craftsmen, for instance in the production of ceramics (Sciau & Goudeau, 2015), often led to very complex structures and composite systems of chemically close phases, which require significant instrumental developments and suitable strategies to describe thoroughly their whole structure. In addition to conventional analytical methods, such as Raman spectroscopy, scanning electron microscopy (SEM) or X-ray diffraction (XRD), it can sometimes be necessary to complement these studies with nanoscale investigations to obtain an in-depth understanding of the materials composing the artefacts (Sciau & Godet, 2021). These data are essential to the comprehensive understanding of the chemical processes taking place during manufacturing.

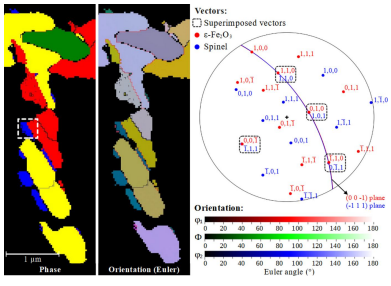

Transmission electron microscopy (TEM) is perfectly suited to reach such scales and precisely characterize complex nanometric structures (Sciau, 2016). Its inherent coupling with electron diffraction and the possibility to implement energy-dispersive spectroscopy (EDS) allows both crystallographic and elemental characterizations at the nanoscale. Significant advances in transmission mapping techniques have also been made to better visualize the complex arrangements of phases in the structures and improve resolution and accuracy. They are presented later on.

Automated crystal orientation mapping associated with precession electron diffraction (ACOM-PED, also known as ASTAR) is a powerful common mapping technique for crystal identification and orientation studies. In this technique, electron diffraction patterns are collected step by step on a thin sample and analysed offline (Viladot *et al.*, 2013; Rauch & Véron, 2014). The achieved resolution is typically 5 to 1 nm depending on the microscope (Zaefferer, 2011). Although not frequently used in heritage studies, this technique has been successfully applied on heritage samples such as Mayan paintings, Roman glass and Greek glazed ceramic fragments (Nicolopoulos *et al.*, 2019). More recently, another technique named transmission Kikuchi diffraction (TKD) has emerged. It is based on a two-step phenomenon in medium-thickness samples: an incoherent (quasi-elastic) scattering of primary electrons followed by diffraction (coherent scattering), generating Kikuchi bands. Although quite old in terms of experimental demonstration (Woolf *et al.*, 1972), the technique was only recently re-introduced in SEM instruments with standard electron backscatter diffraction (EBSD) equipment (Keller & Geiss, 2012). Since it combines the advantages of a scanning electron microscope (accessibility, ease of use, short acquisition time, large probed areas, online analysis) and a spatial resolution reportedly down to 2 nm (Trimby, 2012), which is comparable to that obtained with TEM, TKD has attracted growing interest for diverse research domains, in particular nanocrystalline and ultra-fine-grain materials, highly deformed materials, corrosion studies and geological samples (Sneddon *et al.*, 2016). Because of the similar nature of their results, the two techniques are often compared against each other in the literature. TKD has been proved more efficient than ACOM-PED for the identification of nanostructures with multiple overlapping grains (Mariano *et al.*, 2020) and to have an angular resolution around 0.5°, corresponding to the better limits of the 0.5–2° range achieved by ACOM-PED (Zaefferer, 2011). The achieved orientation maps have been consequently reported to be more robust. Cross-identification by coupling EDS spectra and TKD data has also been implemented in TKD software to better discriminate between phases with chemical differences but a similar structure; however, dwell time and crowding around the sample have to be managed carefully to obtain enough counts on the EDS detectors. In contrast to ACOM-PED, TKD has not yet been used to study heritage samples to our knowledge.

This work is intended as a case study of nanoscale crystallographic and orientation characterization of complex crystallographic systems, such as the ones found in black-to-brown Chinese glazes, using TKD and ACOM-PED. It focuses on a set of brown-ware recreations, which were manufactured using traditional craftsmanship and minimally processed raw material in order to better understand the manufacturing of such glazes during the Song dynasty (960–1279). These glazes were much appreciated during the Song period (Crick, 2013) and are still highly regarded today, with some exceptional bowls considered national treasures in Japan (Song Ceramics, 1999). Several studies have been carried out on ancient samples and highlighted typical dendritic micro- and nanostructures (Dejoie *et al.*, 2014; Wang *et al.*, 2019, 2021; Wen *et al.*, 2019; Ren *et al.*, 2022). This set of samples was shown to display comparable dendritic structures, which contain two iron oxide polymorphs among other phases: ε-Fe_2O_3 and hematite (α-Fe_2O_3) (Holé *et al.*, 2022).

2. Materials and methods

2.1. Sample presentation

This study focuses on two samples, numbered ZJ-08 and ZJ-07, from a series of modern ceramic samples (ZJ series). They were manufactured in collaboration between the Institute of Silicate Cultural Heritage, Shaanxi University of Science and Technology, Xi'an, and the Yaozhou Kiln Lijia Porcelain Workshop Co. Ltd, Tongchuan. The glazes of the samples are made from the same batch of raw material gathered in Huangbu Town, Tongchuan City, Shaanxi Province, and applied on ceramic pieces by dipping. The samples were then fired in a gas-fuelled shuttle kiln and removed successively from the chamber. In particular, samples ZJ-07 and ZJ-08 were removed from the kiln at the beginning of the cooling step at 1160°C and after the kiln had cooled to room temperature, respectively. More details about the sample manufacturing and the firing conditions are presented elsewhere (Holé *et al.*, 2022).

Samples ZJ-07 and ZJ-08 were selected for this study on the basis of preliminary experiments using XRD and Raman spectroscopy highlighting that only those two from the ZJ series contain ε-Fe_2O_3. Hematite and Fe-containing spinel [$(Mg,Fe)Al_2O_4$] were also detected on the surface of ZJ-08 only (Holé *et al.*, 2022).

In addition to these two modern samples, one archaeological sample (numbered LHP-02) was also analysed in this study. This sample comes from the Luhuaping archaeological site close to Shuiji Town (Jianyang, Nanping, Fujian, China). It was provided by Nanping Jian Kilns Ceramics Research Institute (Nanping, Fujian, China). This sherd presents a typical pattern of brown streaks on a black background, commonly referred to as 'hare's fur' (Mowry *et al.*, 1996).

Photographs of the three samples described here are presented in Fig. S1 (in the supporting information).

2.2. Sample preparation

2.2.1. Preliminary preparation. Specimens of each ceramic sample were cut using a circular diamond saw and placed on

aluminium stubs that were carbon-coated with an EM ACE200 coater (Leica). Silver lacquer was added to create conductive bridges between the coated surface of the ceramic and the stubs to prevent excessive charging effects in the electron microscope. The TEM lamellae were then made directly in the scanning electron microscope with a focused ion beam (FIB) as described hereinafter.

2.2.2. Focused ion beam. Thin sections suited for TEM investigation were prepared using the 'Lift-out' technique (Sciau *et al.*, 2009; Sciau, 2016) in a Helios NanoLab 600i dual beam (Thermofisher) equipped with a Ga ion source. This preparation method was chosen to enable a precise selection of the areas of interest thanks to the backscattered electron detector. Lamellae were prepared parallel to primary branches or perpendicular to secondary branches of the dendritic structures as they were visible from the surface of the sample. After careful selection, the areas of interest were covered with a Pt layer to prevent beam damage, then extracted using a high-energy ion beam (30 kV with high currents of 9.3 then 2.5 nA) and a micro-manipulator, and fixed on a copper grid. They were then thinned using a succession of decreasing-energy beams (from 30 to 8 kV) to obtain lamellae with thicknesses between 80 and 130 nm.

2.3. Analyses and methods

TKD and ACOM-PED, although both based on electron diffraction, rely on different physical processes. As such, the patterns obtained for each pixel using these two technique appear widely different: a series of diffraction spots for ACOM-PED and a net of Kikuchi lines for TKD, which then influence the pattern identification. The comparison of the results obtained by the two techniques, both in terms of phase and orientation mapping, is thus relevant.

2.3.1. Scanning TEM and energy-dispersive X-ray spectroscopy. TEM experiments were carried out using an SM20 field-emission gun (FEG) transmission microscope (Philips) equipped with a scanning TEM (STEM) system at a voltage of 200 kV and with magnifications ranging from ×50 000 to ×150 000. EDS maps were recorded using an SDD detector (Bruker) with an energy resolution of 127 eV at the Mn *Kα* emission and processed using the *Esprit* v1.9 software (Bruker). The elemental compositions were determined from the EDS spectra. Several background elements not coming from the sample were removed from the composition calculation but considered in the fitting in order to have accurate deconvolution of the peaks, such as Pt (from the protective layer), Ga (from the FIB preparation), Cu (from the grid) and Co (from the TEM lenses).

2.3.2. ACOM-PED. ACOM-PED mappings were recorded in the SM20 FEG (Philips) using a DigiSTAR P1000 device (NanoMEGAS) at 200 kV voltage, a 0.7° precession angle and a 10 nm step. The data were processed using the *ASTAR* v2.08 software suite (NanoMEGAS). The module *DiffGen* was used to create a diffraction pattern database for each phase from the same CIFs used to index the TKD patterns, the module *Index* to index the experimental patterns by comparing them with the generated ones, and the module *Mapviewer* to display the processed data and extract the orientation information from them.

2.3.3. TKD. TKD maps where recorded using an EBSD NORDLYS II detector (Oxford Instruments) installed on the Helios NanoLab 600i (Thermofisher). Patterns were recorded using 30 kV voltage, 11 nA current, and 4 mm working distance between the electron beam and the sample. Mapping was implemented with a 25 or 30 nm step and with a Hough resolution of 90. The patterns were indexed using the *AZtec* v3.3 software (Oxford Instruments) and CRY files generated with the *Twist* v5.12.63.0 software (Oxford Instruments) from CIFs available in the International Centre for Diffraction Database (ICDD; https://www.icdd.com/), Inorganic Crystal Structure Database (ICSD; Zagorac *et al.*, 2019)

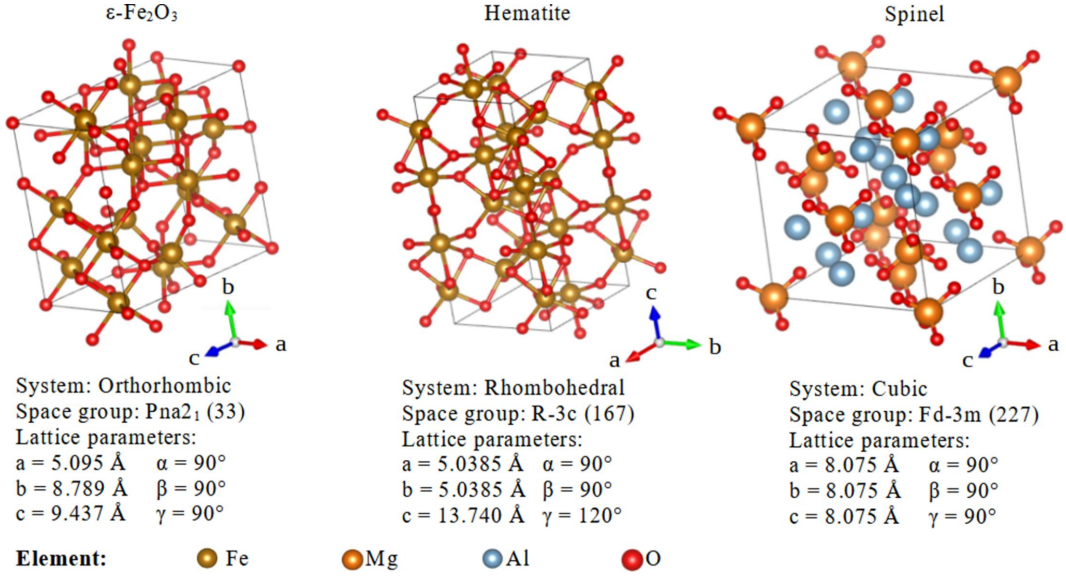

Figure 1
Structures and crystallographic data of ε-Fe_2O_3 (ICSD-51122), hematite (ICDD-01-071-5088) and spinel (COD-1540775).

and Crystallography Open Database (COD; Gražulis *et al.*, 2009). Mappings were reconstructed from the patterns recorded on every pixel using the *Channel5* and *Tango* v5.12.63.0 software (Oxford Instruments). Isolated misindexed pixels were removed using the options available in *Tango* v5.12.63.0.

2.3.4. Orientation data processing. The relationships between the different phases were deduced from TKD and ACOM-PED maps by using the *Misorientation* software from the *Pycotem* software suite (Mompiou & Xie, 2021), which enables the drawing of superposed pole figures of crystals from two different phases. The possibility of epitaxy between different phases suggested by *Misorientation* was studied by displaying the structures given by the CIFs ICSD-51122 for ε-Fe_2O_3 (Tronc *et al.*, 1998), ICDD-01-071-5088 for hematite, COD-1540775 for spinel (Zorina & Kvitka, 1969) and ICDD-00-046-1212 for corundum with the *VESTA 3.5.7* software (Momma & Izumi, 2011) and calculating the O–O distances from these. The structures corresponding to the CIFs of ε-Fe_2O_3, hematite and spinel are displayed in Fig. 1.

2.3.5. XRD and Pawley refinement. 2D diffraction patterns were recorded from the surfaces of the samples using a D8 Discover (Bruker) equipped with an Incoatec IμS 2.0 Co microsource and a Vantec 500 detector (Bruker). Diffractograms were obtained from the 2D images by integration of the signal and the identification of the crystalline phases was done using *DIFFRAC.EVA* software (Bruker) linked with the ICDD. Pawley refinement was implemented using the *TOPAS* software (Bruker; Coelho, 2018) (Pawley, 1980). In addition to the CIFs mentioned in Section 2.3.4, quartz and indialite were detected in the samples and were refined using the structures from the CIFs ICDD-00-046-1045 for quartz and ICDD-01-082-1884 for indialite.

3. Results

3.1. Phase identification in sample ZJ-08

First, to identify efficiently the repartition of the different phases present in the dendrites of sample ZJ-08, elemental analyses were performed. Then, crystallographic studies were implemented using the two electronic diffraction techniques (TKD and ACOM-PED) described above.

Elemental analyses revealed that the dendrites are composed of a complex mixture of grains of four different phases, numbered (1) to (4), intertwined together (Fig. 2).

Phases (1) and (2) contain mainly Fe and have a different amount of Al, according to the obvious contrast visible on the Al mapping. Phase (3) is rich in Mg and Al and phase (4) in Ti and Fe. To better quantify the compositional differences, average chemical compositions of each phase were extracted from several grains of this map and are presented in elemental ratios in Table 1. The EDS spectrum recorded on each labelled grain is presented in Fig. S2.

The Si/O ratio is indicated in the table to give an idea of the influence of the glaze on the recorded compositions. The relatively low Si content in the grains suggests that its influence on the grains is minimal. The elemental ratios measured on the grains of phase (3) are consistent with a spinel phase enriched in Fe of the $(Mg,Fe)Al_2O_4$ type. The ratio measured on phase (4) is consistent with the composition of pseudobrookite, $Fe_2(Ti,Fe)O_5$. The two other phases are ferric oxides, and although their Al content is significantly different, precise identification only with their chemical composition is not possible; therefore, structural identification was performed with TKD and ACOM-PED. The corresponding maps are shown in Fig. 3.

Table 1
Average composition (with standard deviation in parentheses) measured on the grains of different phases.

Elemental ratios	Phase (1)	Phase (2)	Phase (3)	Phase (4)†
Fe/O	43.4% (2.1)	35.2% (1.4)	8.7% (1.3)	29.2%
Al/O	7.0% (0.7)	15.5% (1.1)	36.9% (4.7)	7.7%
Mg/O	0.8% (0.5)	1.2% (0.4)	11.6% (4.4)	1.84%
Ti/O	1.2% (0.4)	0.9% (0.1)	0.05% (0.05)	20.6%
Si/O	0.6% (0.3)	0.7% (0.1)	3.0% (2.0)	0.5%
Fe/Al	6.2% (0.6)	2.3% (0.1)	0.2% (0.1)	3.8%

† No standard deviation is given for phase (4) as there is only one grain of this phase.

The two electron diffraction techniques give comparable results, with only a few minor differences. The first is the lower spatial resolution of the TKD map, which should not be considered for comparison as it represents a compromise between minimizing acquisition time and beam damage on the sample while remaining good enough to allow the mapping of the smallest grains. The second is the presence of edge effects on the ACOM-PED map, which are probably due to a blurring of the diffraction patterns of the grains with the diffusion of the glassy matrix. In addition, the ACOM-PED map allows differentiation of the amorphous Pt deposition from the amorphous glassy matrix.

The two maps confirmed the identification of phases (3) and (4) as spinel and pseudobrookite, respectively, and at the same

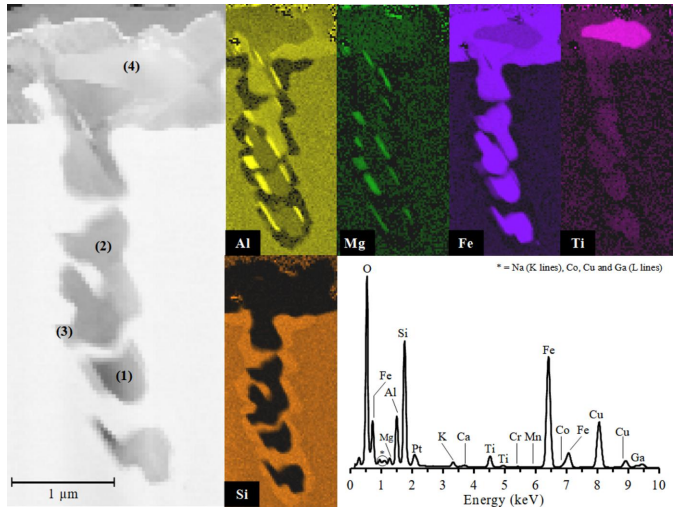

Figure 2
STEM image of a lamella cut perpendicularly to secondary branches of ZJ-08 with associated EDS maps and the average EDS spectrum. Examples of grains of phases (1) to (4) are highlighted on the STEM image.

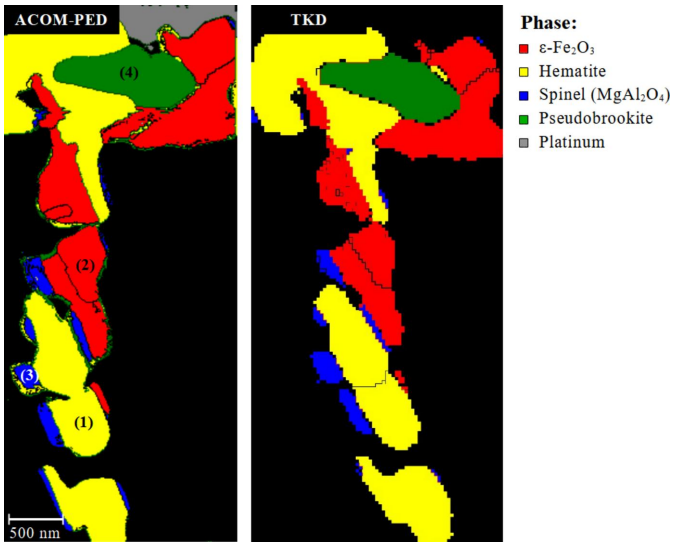

Figure 3
ACOM-PED and TKD phase maps of the area presented in Fig. 2.

time allowed the identification of phase (1) as hematite and phase (2) as ε-Fe_2O_3. Other lamellae taken from different areas of ZJ-08 showed similar phase composition, with the exception of pseudobrookite which is absent for most of them. This is because pseudobrookite comes from the transformation of anatase grains from the raw material in the Fe-rich environment of the glaze (Djuric *et al.*, 2014), which are relatively uncommon in the raw material.

3.2. Limitations

Although the phase maps presented above were very successful and led to the accurate identification of the different phases and grain boundaries, instances of major disagreement between the two methods were observed on another lamella (Fig. 4).

Here the comparison between TKD and ACOM-PED shows major differences in the phase attribution of several grains as well as a drift on the TKD map. Using the EDS compositions as references, it appears on the one hand that the grains identified using TKD have been correctly characterized, but some display unidentified areas or areas that have been completely ignored. On the other hand, ACOM-PED proposed an identification for every grain, but happens to be sometimes wrong, as it contradicts the EDS data.

These differences can be explained by several factors, which are mainly related to the sample preparation. This step is crucial, as it enables analyses to be performed in the best conditions, but can be particularly tricky for heritage ceramics such as in this case. FIB preparation was chosen instead of more conventional preparation as the ceramics studied here have well developed dendritic structures which require a careful selection of the sampling area to be studied. FIB enables such precise selection, with the additional advantages of requiring minor prior preparation (identical to SEM samples) and impacting a small area of the sample (typically in the 20 μm^2 range).

However, the intrinsic heterogeneity and composite nature of ancient ceramics complicate the thinning of the lamellae. The hardness differences between the glassy matrix and the crystals lead to a typical curtaining effect which results in an uneven thickness of the lamellae. The presence of bubbles trapped in the glaze or cracks can also drastically affect the thickness, resulting even sometimes in holes in the lamellae. In contrast to modern materials, which can be relatively easy to synthesize again to prepare better samples, archaeological material is limited and cannot be crafted again due to its unique nature. The multiplication of the sampling for additional preparation is also generally impossible for the same reasons. This implies that the archaeological samples have to be studied such as they are, with all the limitations described above.

The poor control of the thickness of the lamellae may lead to issues for electron diffraction analyses. Indeed, the results of TKD analyses are influenced by the thickness of the sample (Liu *et al.*, 2019). This is due to the two-step physical process behind the technique, consisting first of an incoherent scattering of the primary beam, followed by coherent scattering of the forward biased electrons: on the one hand, if the lamella is too thin, the second step of the process cannot happen; on the other hand, if the lamella is too thick, there is a higher chance of the coherently scattered electron scattering incoherently once more and thus not contributing to the pattern. The detection of the crystals is also influenced by this two-step phenomenon, as the grains located in the first part of the lamella, where the first incoherent scattering happens, will not be detected: only the grains in the second part will coherently scatter the beam and create the diffraction patterns (Liu *et al.*, 2019). Although ACOM-PED is not affected as much as TKD as long as the lamella is transparent to electrons, a higher thickness may result in grain superposition inside the lamella. This creates a combined pattern of the superposed grains which is wrongly attributed to one phase by the software; this

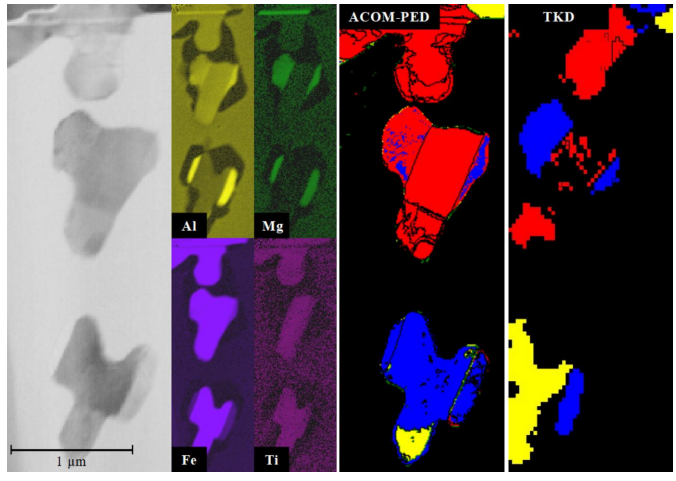

Figure 4
STEM image of a lamella cut perpendicularly to secondary branches of ZJ-08 with associated EDS maps with corresponding ACOM-PED and TKD phase maps (colour legend identical to that in Fig. 3: ε-Fe_2O_3 in red, hematite in yellow and spinel in blue).

is a commonly reported error in ACOM-PED (Mariano *et al.*, 2020). These grains can, however, be easily identified in most cases thanks to their poor reliability index. This index is calculated by the *ASTAR* software when indexing the patterns of each pixel and decreases when the pattern can be indexed with more than one solution (Viladot *et al.*, 2013).

It is thus crucial to consider these limitations when analysing complex samples. Since TKD and ACOM-PED are not affected in the same way, one technique can be better suited than the other, depending on the sample. The use of both techniques on the same sample can then be relevant, highlighting the problematic areas and confirming at the same time the accurate identifications. Coupling these with other techniques, such as STEM-EDS, also proved to be a very relevant check when phases were misidentified as other phases whose chemical compositions are not the same, for instance when hematite was identified as spinel.

3.3. Orientation studies in sample ZJ-08

In addition to the identification of the phases, these data also provide orientation information about the different crystalline phases. The TKD orientation map (Fig. 4) shows that each crystalline species grows in specific orientations: all spinel grains have the same orientation (dark blue), hematite grains have two orientations only (lavender purple and greenish beige) and ε-Fe_2O_3 have three orientations (grey and two shades of brownish green).

In addition to the organized orientation of the grains of each species, the presence of planar boundaries between the different species could suggest the existence of a relationship between the three phases. The potential relationship can be investigated directly by extracting the Euler angles of two neighbouring grains given by both diffraction techniques and drawing the associated pole figure superposed together on the same figure. This process makes possible the direct identification of parallel axes between the two oriented grains, and the deduction of possible shared planes, as shown for instance with a grain of spinel and one of phase ε-Fe_2O_3 (Fig. 5).

This method applied to every set of neighbouring grains of different nature enabled the identification of one family of planes for each phase that could be shared with the others, namely the planes (001) of the ε-Fe_2O_3 phase and (0001) of the hematite with [100] and [10$\bar{1}$0] being co-linear in-plane vectors, planes (00$\bar{1}$) of the ε-Fe_2O_3 and (111) of the spinel with [100] and [1$\bar{1}$0] being co-linear in-plane vectors, and (0001) of the hematite and (111) of the spinel with [2$\bar{1}$10] and [1$\bar{1}$0] being co-linear in-plane vectors. A similar relationship between spinel and ε-Fe_2O_3 was found in a rhombus-shaped particle from Japanese Bizen stoneware glaze, which is composed of these two oxides presenting the [111] zone axis of the spinel parallel to [001] of ε-Fe_2O_3 according to TEM-SAED (selected-area electron diffraction) (Kusano *et al.*, 2021).

By examining the crystal structures of the three oxides along the directions mentioned above, it appears obvious that all the shared planes exhibit a pseudo-hexagonal array of oxygen atoms (Fig. 6). With the known lattice parameters given by the CIFs mentioned in Section 2.3 and the positions of the oxygen atoms in the structure, the average O–O distance can be calculated, giving 2.936 Å for the ε-Fe_2O_3 phase, 2.909 Å for the hematite and 2.855 Å for the spinel.

The corresponding lattice mismatch (in this case, the linear mismatch) between the structures (Gu, 2020) was calculated: 2.80% between the ε-Fe_2O_3 phase and the spinel, 0.92% between the ε-Fe_2O_3 phase and the hematite, and 1.87% between the hematite phase and the spinel. As a mismatch lower than 5% is generally considered to allow epitaxial growth of one species on another (Nahhas *et al.*, 2001; Liu & Zhang, 2020), the situation appears therefore favourable for epitaxial growth of hematite and spinel on ε-Fe_2O_3 in this case.

To further document the epitaxial relationships in this case, where the ε-Fe_2O_3 phase is significantly substituted with Al, a Pawley refinement was implemented on an XRD pattern recorded on ZJ-07 (Fig. S3). This refinement determined the lattice parameters to be smaller than those calculated by Tronc *et al.* (1998), at a = 5.079 (2), b = 8.690 (3) and c = 9.378 (2) Å, which corresponds to a lattice volume difference of 2.1%. The resulting cell shrinkages lead to smaller O–O distances, which

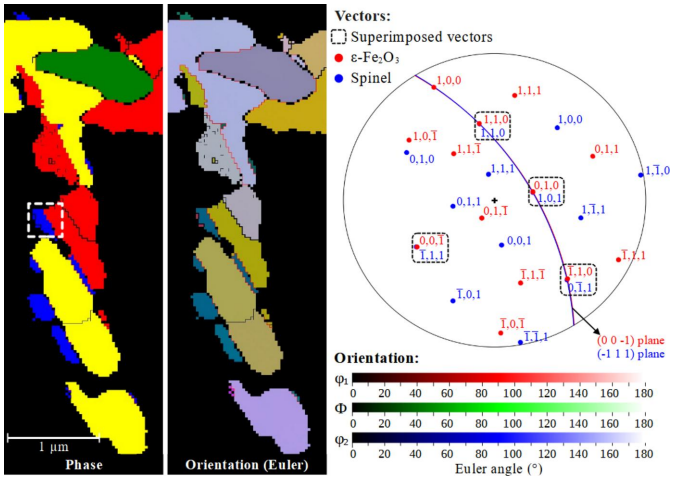

Figure 5
TKD phase map (colour legend identical to that in Fig. 3: ε-Fe_2O_3 in red, hematite in yellow, spinel in blue and pseudobrookite in green) and associated orientation in Euler angles. Pole figure representing the orientation of the two crystals from the boxed area (white dashed lines). Planes (00$\bar{1}$) of ε-Fe_2O_3 and ($\bar{1}$11) of spinel are represented in red and blue, respectively.

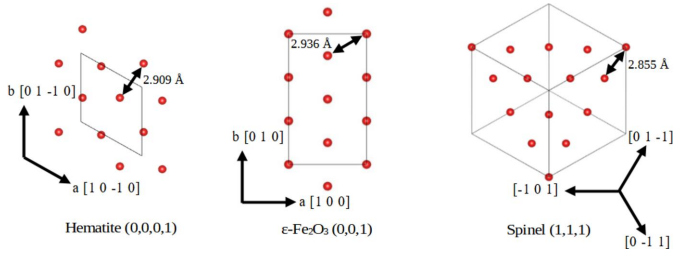

Figure 6
Hematite, ε-Fe_2O_3 and spinel planes with pseudo-hexagonally arranged oxygen atoms.

themselves lead to lower mismatches between the phases. For instance, considering the calculated lattice parameters of Al-substituted ε-Fe_2O_3, the mismatch between this phase and spinel becomes 1.28%, less than half the 2.80% previously calculated with pure ε-Fe_2O_3. Similar trends in the lattice parameters were observed in Al-substituted hematite crystals found in *terra sigillata* ceramics, which would also decrease the mismatches between hematite and spinel (Sciau *et al.*, 2006). The Al substitution thus favours the epitaxial growth of hematite and spinel.

3.4. Comparison of samples ZJ-07 and LHP-02

Sample ZJ-07 presents a much simpler composition, containing only ε-Fe_2O_3 (Fig. 7, left), in agreement with a previous study that used other analytical techniques (Holé *et al.*, 2022). The few pixels which are not identified as ε-Fe_2O_3 in this map are due to edge effects, as discussed previously. It is noteworthy that all crystals display exactly the same crystalline orientation. This fact indicates that all branches grew in the same direction as in a very coherent dendritic system (Fig. 7, right).

As the only difference between this sample and ZJ-08 is that it was removed from the chamber of the kiln earlier during cooling (at 1160°C), this analysis confirms that hematite and spinel crystallize at a lower temperature compared with ε-Fe_2O_3.

The dendritic structures of ZJ-07 are very similar to those found in ancient samples, which also have a mono-phasic composition with all branches oriented in the same direction, as illustrated by the TKD mapping implemented on LHP-02 shown in the supporting information (*cf.* Fig. S4).

4. Discussion

4.1. Hematite and spinel

Sample ZJ-07, which was removed from the kiln at 1160°C during cooling, contains already well developed dendrites exclusively composed of ε-Fe_2O_3, without hematite or spinel (Holé *et al.*, 2022). On the other hand, ZJ-08, which was removed later at the end of the cooling, contains hematite and spinel in addition to ε-Fe_2O_3. This difference between the two samples indicates that the growth of hematite and spinel occurs at a lower temperature than for ε-Fe_2O_3, which begins to crystallize at temperatures above 1160°C.

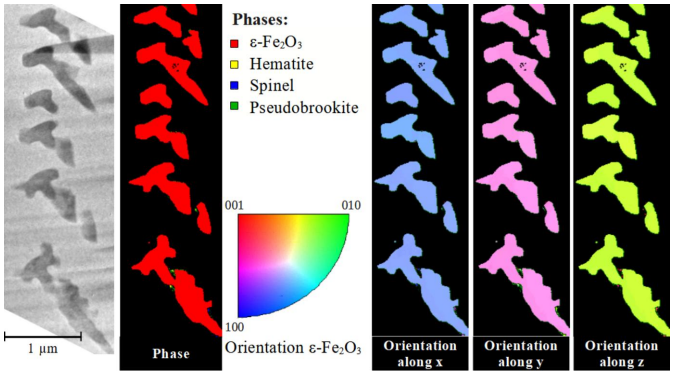

Figure 7
TEM image of a lamella cut perpendicularly to secondary branches of ZJ-07 with corresponding ACOM-PED phase and orientation maps in crystal orientations relative to the sample (the surface of the sample is to the left of the pictures).

The stability of ε-Fe_2O_3 has been regularly discussed in the literature, in particular regarding the successive transformations γ-$Fe_2O_3 \rightarrow \varepsilon$-$Fe_2O_3 \rightarrow \alpha$-$Fe_2O_3$ (Lee & Xu, 2016). On the one hand, the transformation of ε-Fe_2O_3 into hematite has been shown to occur with the increase in the size of particles due to the lower surface energy (Gich *et al.*, 2007; Sakurai *et al.*, 2009; Machala *et al.*, 2011; Ohkoshi & Tokoro, 2013; Lee & Xu, 2016). On the other hand, temperature plays a crucial role, as hematite is more stable than ε-Fe_2O_3 at lower temperature, and annealing of ε-Fe_2O_3 particles usually sparks their transformation into hematite (Lee & Xu, 2016; Nikolić *et al.*, 2017).

Although pure ε-Fe_2O_3 particles have sizes reported to be in the nano range, particles found in ancient Chinese glazes regularly exceed 1 µm. It has been hypothesized that these impressive sizes are possible due to Al substitution stabilizing the bigger particles (Wang *et al.*, 2021). The possible range of Al substitution in ε-Fe_2O_3 has also been shown to be very wide (Yamada *et al.*, 2012; Nasu *et al.*, 2017).

The presence of both hematite and ε-Fe_2O_3 phase in the dendrites of sample ZJ-08 might be explained by two different mechanisms, which are discussed below: the decomposition of ε-Fe_2O_3 into hematite and spinel during cooling or the epitaxial growth of the two phases on ε-Fe_2O_3.

Mechanism 1: transformation of the Al-containing ε-Fe_2O_3 into hematite and spinel. If one considers that, despite the massive Al substitution in the ε-Fe_2O_3 of brown glazes, the stability difference between hematite and ε-Fe_2O_3 is still significant, the ε-$Fe_2O_3 \rightarrow \alpha$-$Fe_2O_3$ transformation could still take place in the glaze during cooling, as in the studies implemented on pure ε-Fe_2O_3 discussed above. Indeed, the crystal size increases and the temperature decreases during this step, both phenomena favouring hematite over ε-Fe_2O_3 from a thermodynamic point of view. However, the very high Al content measured in ε-Fe_2O_3 (Fe/Al = 6.2) is impossible to maintain in hematite at temperatures below 1160°C (Feenstra *et al.*, 2005), which would be the case for the sample studied here. To give a numerical example, the minimal Fe/Al ratio in hematite at 1000°C under atmospheric pressure would be 9 according to Feenstra *et al.*, significantly higher than the present value. Al would then have to be eliminated from the structure to allow the transformation into hematite.

To eliminate Al from the hematite structure, the precipitation of corundum would seem to be a good candidate. However, the average O–O distance in the pseudo-hexagonally arranged oxygen atom (0001) planes of corundum can be estimated to be 2.748 Å, which would result in a lattice mismatch of 6.62% with ε-Fe_2O_3 and 5.69% with hematite. These values are above 5%, which means that epitaxial growth of corundum is not favoured. In contrast, the epitaxial growth of spinel is favoured according to the lattice mismatch (as discussed in Section 3.3). This, and the relatively high Mg content in the glaze (around 3.0 wt%) (Holé *et al.*, 2022),

would lead to growth of spinel (a very stable phase indeed) instead of corundum to eliminate the excess of Al in the iron oxides during the transformation ε-$Fe_2O_3 \rightarrow \alpha$-$Fe_2O_3$.

Mechanism 2: growth of hematite and spinel on existing Al-containing ε-Fe_2O_3. If one considers now that the Al substitution in the ε-Fe_2O_3 crystals observed in the glaze stabilizes them enough to prevent their transformation while at high temperature, the cooling would still have an influence on the growth of new crystals.

According to the temperature/particle-size diagram for Fe_2O_3 presented by Lee & Xu (2016), it is clear that hematite is more stable than ε-Fe_2O_3 below 1100°C for particle sizes above 250 nm. As shown in Figs. 2 and 3, the particle size in the glaze is larger, being in the 300–1000 nm range and thus in the zone where hematite is more stable. As the temperature continues to decrease, hematite becomes increasingly more stable compared with ε-Fe_2O_3, resulting in its epitaxial crystallization on the existing ε-Fe_2O_3 crystals. The lower solubility of Al in hematite results in an increasing concentration of this element in the surrounding glassy matrix. This high Al concentration, coupled with the naturally high Mg content of the glaze and the favourable crystallographic conditions, allows epitaxial growth of spinel alongside hematite.

These two mechanisms, illustrated in Fig. 8, could plausibly explain the co-existence of hematite, spinel and ε-Fe_2O_3 in the glaze of sample ZJ-08 while only ε-Fe_2O_3 is present in sample ZJ-07. These mechanisms are not mutually incompatible and it is possible that both happen simultaneously. It is important to keep in mind that these propositions are based on local observation of different dendrites of the samples, which represent the initial and final stages of the transformation. The successful electron diffraction measurements allowed a detailed characterization at the nanoscale which makes it possible to propose such mechanisms. To get a more complete understanding of the growth of such structures, additional experiments have to be implemented, taking into account the influence of the local composition or the atmosphere for instance, but that was not the aim of this work.

Finally, the presence of a grain of pseudobrookite, without any epitaxial relationship with other phases in the lamella presented, is most likely due to the local presence of a titanium oxide grain playing the role of a precursor, such as anatase which was identified in the raw material (Holé *et al.*, 2022) or rutile which would result from its prior transformation at high temperature (Shannon & Pask, 1965; Djuric *et al.*, 2014).

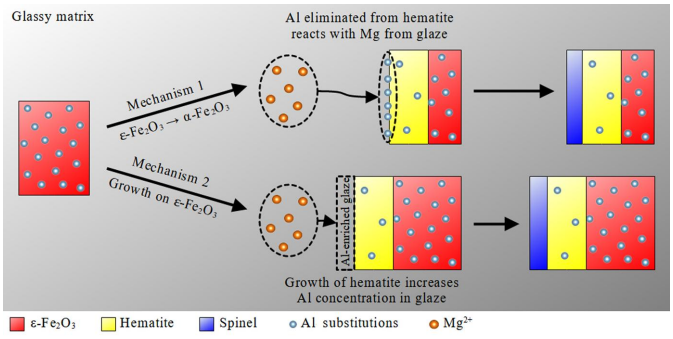

Figure 8
Graphical representation of the two possible mechanisms for the presence of both hematite and ε-Fe_2O_3 phases in sample ZJ-08.

4.2. Comparison with the archaeological sample

The multi-phase dendrites of samples ZJ-08 display major differences compared with the archaeological sample LHP-02, whereas sample ZJ-07 is very similar to the latter. These differences suggest that the cooling conditions to which this sample was exposed may have been better suited for freezing the high-temperature structures containing only ε-Fe_2O_3. A slower cooling at high temperatures for instance may favour the homogeneous development of the ε-Fe_2O_3 dendrites and sufficiently deplete the glassy matrix of Fe to prevent further growth at lower temperature where these structures would become less stable. However, one should be cautious as the composition of the raw material may also drastically influence the chemistry of the glassy matrix and thus influence the crystallization processes of the samples from the ZJ series and LHP-02.

5. Conclusion

We have studied the complex dendritic structures found in Chinese brown glazes using two electron diffraction mapping techniques (TKD and ACOM-PED). Some differences were observed between TKD and ACOM-PED, which can be explained by the different physical phenomena behind the two techniques and the difficult process of sample preparation. The latter can influence the former, as the results of the analyses depend on the thickness of the lamellae; sample preparation is especially limiting in the case of archaeological material. This may result in non-ideal conditions in which to perform the analyses; however, accurate identification is possible, as proven here. This study also highlighted epitaxial relationships between the families of planes (001) of ε-Fe_2O_3, (0001) of hematite and (111) of spinel on the modern sample which remained in the kiln throughout the firing. The presence of the two latter phases can be explained by the transformation of Al-substituted ε-Fe_2O_3 into hematite and spinel and/or the growth of hematite and spinel on existing ε-Fe_2O_3 crystals stabilized by their Al substitution as the temperature decreases. Such phases are not present in the archaeological sample, which is very similar to the modern sample removed from the kiln at 1160°C during cooling. This suggests a difference between the chamber cooling during the Song dynasty and that used for the manufacturing of these samples.

Acknowledgements

The authors of this paper thank Shuanmin Ren from the Tongshuan Yaozhou Kiln Lijia Porcelain Workshop Co. Ltd for manufacturing the sample set ZJ. They also gratefully acknowledge Cécile Marcelot for her help in the recording of the STEM-EDS data, Robin Cours for his advice and

expertise in relation to the FIB sample preparation, and Frederic Mompiou for his guidance with the *pycotem* software suite, all three from CNRS, CEMES. Finally, they thank Arnaud Proietti from the Centre de Microcaractérization Raimond Castaing for his help with the TKD experiments. The authors of this study declare no conflict of interest.

Funding information

This study was performed in the framework of the research collaboration agreement (CNRS No. 186116) between the French National Centre for Scientific Research and the Shaanxi University of Science and Technology. It has been financed by the centralized thesis programme of the CNRS Directorate General for Science (80PRIME, Thèses transverses).

References

Coelho, A. A. (2018). *J. Appl. Cryst.* **51**, 210–218.
Crick, M. (2013). *La Céramique Impériale Song: Sobriété, Élégance et Perfection Technique*. Bulletin No. 73, Editions Baur. Genève: Fondation Baur-Musée des Arts d'Extrême Orient.
Dejoie, C., Sciau, P., Li, W., Noé, L., Mehta, A., Chen, K., Luo, H., Kunz, M., Tamura, N. & Liu, Z. (2014). *Sci. Rep.* **4**, 4941.
Djuric, Z. Z., Aleksic, O. S., Nikolic, M. V., Labus, N., Radovanovic, M. & Lukovic, M. D. (2014). *Ceram. Int.* **40**, 15131–15141.
Feenstra, A., Sämann, S. & Wunder, B. (2005). *J. Petrol.* **46**, 1881–1892.
Gich, M., Roig, A., Taboada, E., Molins, E., Bonafos, C. & Snoeck, E. (2007). *Faraday Discuss.* **136**, 345.
Gražulis, S., Chateigner, D., Downs, R. T., Yokochi, A. F. T., Quirós, M., Lutterotti, L., Manakova, E., Butkus, J., Moeck, P. & Le Bail, A. (2009). *J. Appl. Cryst.* **42**, 726–729.
Gu, X. (2020). *Crystals*, **10**, 192.
Holé, C., Ren, Z., Wang, F., Zhu, J., Wang, T. & Sciau, P. (2022). *Mater. Today Commun.* **33**, 104329.
Keller, R. R. & Geiss, R. H. (2012). *J. Microsc.* **245**, 245–251.
Kusano, Y., Nakata, H., Peng, Z., Maki, R. S. S., Ogawa, T. & Fukuhara, M. (2021). *Appl. Mater. Interfaces*, **13**, 38491–38498.
Lee, S. & Xu, H. (2016). *J. Phys. Chem. C*, **120**, 13316–13322.
Liu, J., Lozano-Perez, S., Wilkinson, A. J. & Grovenor, C. R. M. (2019). *Ultramicroscopy*, **205**, 5–12.
Liu, J. & Zhang, J. (2020). *Chem. Rev.* **120**, 2123–2170.
Machala, L., Tuček, J. & Zbořil, R. (2011). *Chem. Mater.* **23**, 3255–3272.
Mariano, R. G., Yau, A., McKeown, J. T., Kumar, M. & Kanan, M. W. (2020). *ACS Omega*, **5**, 2791–2799.
Momma, K. & Izumi, F. (2011). *J. Appl. Cryst.* **44**, 1272–1276.
Mompiou, F. & Xie, R. (2021). *J. Microsc.* **282**, 84–97.
Mowry, R. D., Farrell, E. & Coolidge Rousmaniere, N. (1996). *Hare's Fur, Tortoiseshell, and Partridge Feathers: Chinese Brown- and Black-Glazed Ceramics*, pp. 400–1400. Harvard University Art Museums.
Nahhas, A., Kim, H. K. & Blachere, J. (2001). *Appl. Phys. Lett.* **78**, 1511–1513.
Nasu, T., Yoshikiyo, M., Tokoro, H., Namai, A. & Ohkoshi, S. (2017). *Eur. J. Inorg. Chem.* **2017**, 531–534.
Nicolopoulos, S., Das, P. P., Pérez, A. G., Zacharias, N., Cuapa, S. T., Alatorre, J. A. A., Mugnaioli, E., Gemmi, M. & Rauch, E. F. (2019). *Scanning*, **2019**, 4870693.
Nikolić, V. N., Tadić, M., Panjan, M., Kopanja, L., Cvjetićanin, N. & Spasojević, V. (2017). *Ceram. Int.* **43**, 3147–3155.
Ohkoshi, S. & Tokoro, H. (2013). *Bull. Chem. Soc. Jpn*, **86**, 897–907.
Pawley, G. S. (1980). *J. Appl. Cryst.* **13**, 630–633.
Rauch, E. F. & Véron, M. (2014). *Mater. Charact.* **98**, 1–9.
Ren, Z., Wang, F., Hole, C., Sciau, P., Shi, P., Zhu, J., Luo, H., Li, Q. & Wang, T. (2022). *J. Eur. Ceram. Soc.* **42**, 7352–7359.
Sakurai, S., Namai, A., Hashimoto, K. & Ohkoshi, S. (2009). *J. Am. Chem. Soc.* **131**, 18299–18303.
Sciau, P. & Godet, M. (2021). *Spectroscopy, Diffraction and Tomography in Art and Heritage Science.* Ghent: Elsevier.
Sciau, P. & Goudeau, P. (2015). *Eur. Phys. J. B*, **88**, 132.
Sciau, P., Relaix, S., Roucau, C., Kihn, Y. & Chabanne, D. (2006). *J. Am. Ceram. Soc.* **89**, 1053–1058.
Sciau, Ph. (2016). *Advances in Imaging and Electron Physics*, edited by P. W. Hawkes, Vol. 198, pp. 43–67. Cambridge, San Diego, Kidlington, London: Elsevier.
Sciau, Ph., Salles, Ph., Roucau, C., Mehta, A. & Benassayag, G. (2009). *Micron*, **40**, 597–604.
Shannon, R. D. & Pask, J. A. (1965). *J. Am. Ceram. Soc.* **48**, 391–398.
Sneddon, G. C., Trimby, P. W. & Cairney, J. M. (2016). *Mater. Sci. Eng. Rep.* **110**, 1–12.
Song Ceramics (1999). *Catalogue des Exposition Tobu Bijutsukan (Tokyo), Osaka Shiritsu Tôyô Tôji Bijutsukan (Osaka) et Yamaguchi Kenritsu Hagi Bijutsukan Uragami Kinenkan (Hagi)*. Tokyo, Osaka, Habi.
Trimby, P. W. (2012). *Ultramicroscopy*, **120**, 16–24.
Tronc, E., Chanéac, C. & Jolivet, J. P. (1998). *J. Solid State Chem.* **139**, 93–104.
Viladot, D., Véron, M., Gemmi, M., Peiró, F., Portillo, J., Estradé, S., Mendoza, J., Llorca-Isern, N. & Nicolopoulos, S. (2013). *J. Microsc.* **252**, 23–34.
Wang, L., Wang, Y., Zhang, M., Li, Q., Wu, J., Liu, Z., Li, L. & Wei, X. (2019). *Anal. Chem.* **91**, 13054–13061.
Wang, T., Hole, C., Ren, Z., Zhang, P., Shi, P., Zhu, J., Luo, H., Wang, F. & Sciau, P. (2021). *J. Eur. Ceram. Soc.* **41**, 6049–6058.
Wen, R., Wang, D., Wang, L. & Dang, Y. (2019). *Ceram. Int.* **45**, 10589–10595.
Woolf, R. J., Joy, D. C. & Tansley, D. W. (1972). *J. Phys. E Sci. Instrum.* **5**, 230–233.
Yamada, K., Yoshikiyo, M., Namai, A. & Ohkoshi, S. (2012). *Hyperfine Interact.* **205**, 117–120.
Zaefferer, S. (2011). *Cryst. Res. Technol.* **46**, 607–628.
Zagorac, D., Müller, H., Ruehl, S., Zagorac, J. & Rehme, S. (2019). *J. Appl. Cryst.* **52**, 918–925.
Zorina, N. G. & Kvitka, S. S. (1969). *Kristallografiya*, **13**, 599–600.